

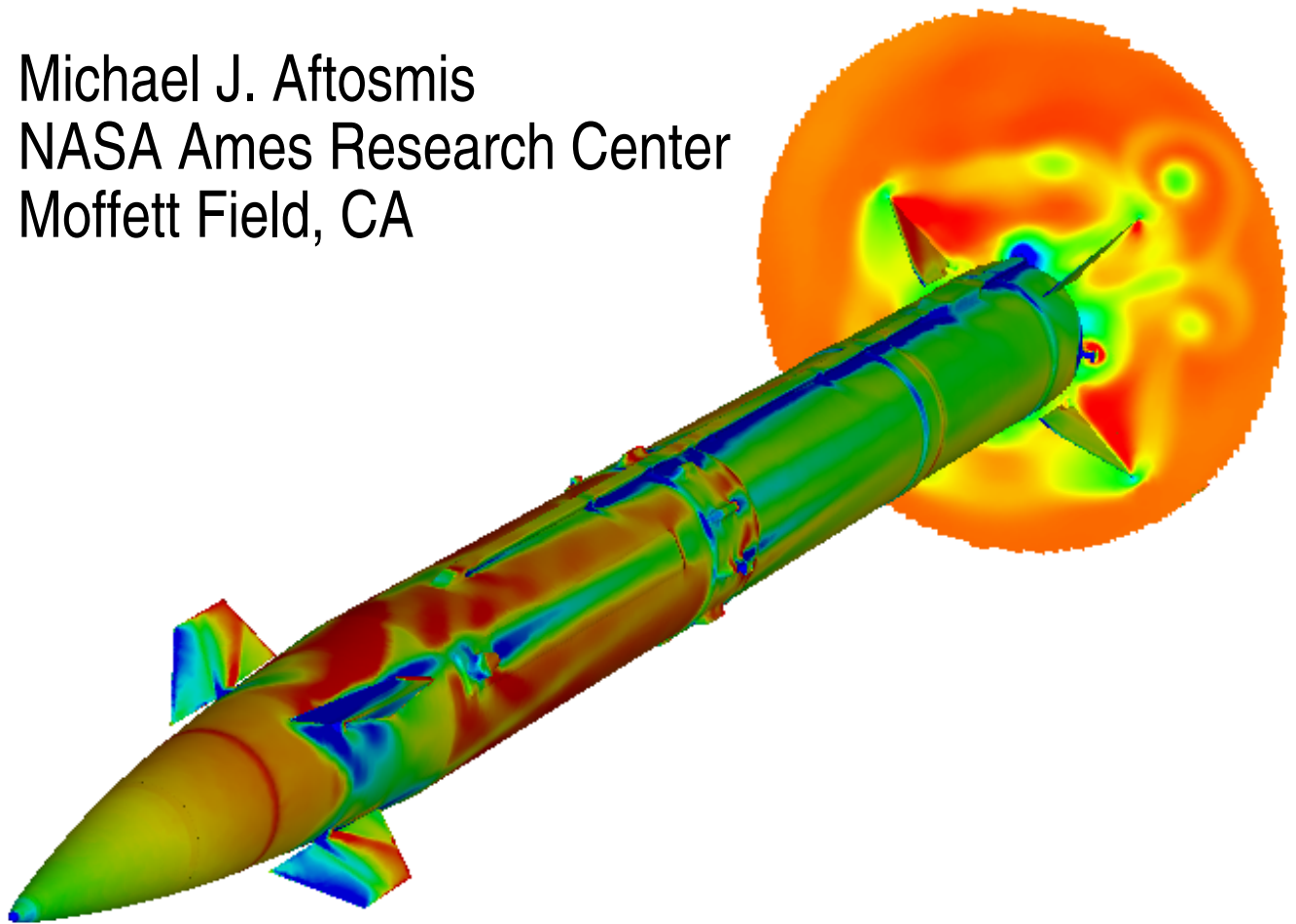


AIAA-2003-3670

**Cartesian-Grid Simulations of a
Canard-Controlled Missile with a Spinning Tail**

Scott M. Murman
ELORET
Moffett Field, CA

Michael J. Aftosmis
NASA Ames Research Center
Moffett Field, CA



21st AIAA Applied Aerodynamics Conference

June 23-26, 2003 / Orlando, FL

Cartesian-Grid Simulations of a Canard-Controlled Missile with a Spinning Tail

Scott M. Murman*
ELORET
MS T27B
Moffett Field, CA 94035
smurman@nas.nasa.gov

Michael J. Aftosmis†
NASA Ames Research Center
MS T27B
Moffett Field, CA 94035
aftosmis@nas.nasa.gov

Abstract

The paper presents a series of simulations of a geometrically-complex, canard-controlled, supersonic missile with free-spinning tail fins. Time-dependent, relative-motion simulations were performed using an inviscid Cartesian-grid-based method at three angles of attack. Two methods of modeling the spinning tail section are compared; an imposed tail spin rate such that the net rolling moment on the empennage is zero, and a free-to-spin configuration using a constrained 6-DOF motion. Computational results are compared with high-resolution Navier-Stokes computations. The results indicate that the choice of a static, forced-spin, or free-to-spin analysis cannot in general be made a priori. Further, the behavior of the dynamic tail section is likely multi-valued, and hence the state for any configuration is dependent upon the past history of the missile.

1 Introduction

Over the past decade, static Computational Fluid Dynamics (CFD) simulations over increasingly complex vehicles have become commonplace. In this evolution, non-body-fitted Cartesian grid methods have proven to be particularly useful for automatically meshing geometrically-complex vehicles[1–6]. Recently this class of meshing and solution techniques has been extended to dynamic simulations[7–10], where components of the geometry move in some manner *during* the simulation. This makes highly-automated simulations of complex three-dimensional vehicles with components in relative motion more feasible. The current work adopts a non-body-fitted Cartesian method to study the performance of a supersonic, canard-controlled missile with a free-spinning tail. On this type of vehicle, the tail fins are free to spin as a unit

around the missile longitudinal axis. As a result, torque from aerodynamic loads on the empennage causes the fin system to spin, even under steady-state flight conditions.

Missiles with dynamic components can pose significant challenges for numerical simulation. In the present example, the spinning tail is a by-product of the forces on the missile and is integral to its aerodynamic performance. Nevertheless, the performance of the missile is often characterized by the spin-averaged aerodynamic coefficients, and hence time-dependent, moving-body simulations are required to predict even *static* stability and control (S&C) information.* Moreover, the spin-rate of the fin system is governed not only by the wind vector and canard deflections, but also by the strength and location of the convected canard vortices, whose induced velocity field differentially loads the tail fins at low angles of attack. The need to convect the canard vortices over the length of the missile to interact with the fin system directly impacts the size of the computational mesh required for ac-

*Senior Research Scientist, Member AIAA

†Research Scientist, Senior Member AIAA

Copyright ©2003 by the American Institute of Aeronautics and Astronautics, Inc. The U. S. Government has a royalty-free license to exercise all rights under the copyright claimed herein for Governmental purposes. All other rights are reserved by the copyright owner.

*Static here means the absence of higher-order dynamic stability derivatives, but does still include spinning tail section.

curate numerical simulation. The combination of these factors makes for CPU-intensive simulations since the physics requires both highly-resolved spatial grids and time-dependent, moving-body solution methodologies.

The paper details the missile geometry under consideration, important features of the computational mesh, and the numerical method used for the simulations. The numerical investigations first concentrate on the flowfield at $\alpha = 4.0^\circ$, where the canard/tail interactions are strongest, and the spin rate of the tail is expected to be highest. Steady-state simulations of the missile with the fins fixed at various azimuths around the missile axis establish a zero-spin-rate baseline. Dynamic simulations are then performed with an imposed spin rate on the tail. An iterative process is used to determine the spin rate which predicts a zero spin-averaged torque on the tail. These fixed spin rate simulations are compared with free-to-spin simulations obtained using a coupled CFD/6-DOF approach. The computational results are compared with highly-resolved Navier-Stokes numerical simulations[11]. The final section extends the analysis by considering the variation of tail behavior with angle of attack for fixed canard settings. The static, forced-spin, and free-to-spin analyses are all used to provide detailed insight into the complex dynamic behavior of the tail.

2 Numerical Method

2.1 Geometry and Computational Mesh

Figure 1 shows three views of the canard-controlled missile used for this study. The missile is depicted with the tail in the + position, corresponding to a tail rotation angle of $\phi_{tail} = 45^\circ$. Zero rotation angle is obtained when the tail is in the \times position, and positive rotation is clockwise when observed from the missile nose. The canards are shown in their deflected position – pitched asymmetrically with $\delta_c = 16^\circ$ to command a starboard yaw of the missile. The missile body has a cylindrical cross-section with a fineness ratio (length/diameter ratio) of about 15.0. Two conduits, which are raised off the body and anchored at regular intervals leaving a small gap, run the length of the body. In addition, the missile has a ring of 10 bluff protuberances at roughly the mid-station

of the body, and several others at the aft end near the free-spinning tail fins. The leading edges of the fins extend forward along the body, and the root station is cutaway to clear both the conduits and other hardware as the fins sweep over the missile body. The minimum clearance is about 1/8th of the fin thickness, and occurs when the fin passes over the protuberances on the aft missile body.

Detailed enlargements of the surface triangulation near the nose, mid-body and tail fins are shown in Fig. 2. The tail is in the + position which puts the upper and lower fins over two of the conduits and the other two fins over protuberances in the aft missile forebody. This triangulation was produced directly from CAD solids without requiring any user input using the automatic triangulation software described in [12]. This software uses the CAPRI library[13, 14] to access the CAD geometry using the CAD system’s native query routines and geometry engine. The final triangulation (shown) uses approximately 400,000 triangles which were used as input to the Cartesian mesh generation system[5].

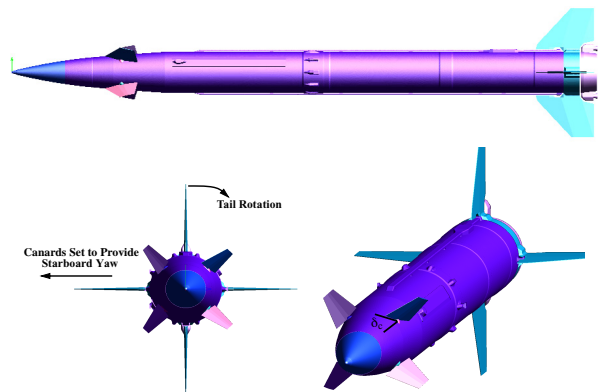


Figure 1: Front, side and isometric view of generic missile with free-spinning tail. For the simulations presented, all 4 canards are deflected $\delta_c = 16^\circ$ to command a starboard yaw of the missile. The tail is shown in the + configuration which corresponds to a tail rotation angle, $\phi_{tail} = 45^\circ$. $\phi_{tail} = 0^\circ$ is obtained with the empennage in the \times position.

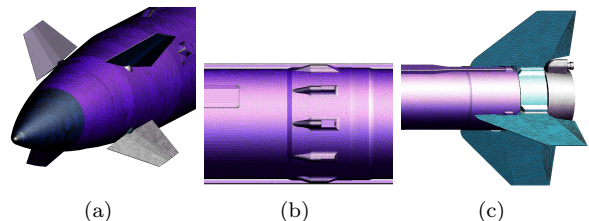


Figure 2: Surface mesh detail of missile configuration, 400,000 triangles.

Figure 3 shows the non-body-fitted baseline Cartesian mesh used for the simulations. This figure shows the tail fin in the \times position ($\phi_{tail} = 0^\circ$), and the mesh is displayed by several cutting planes behind and perpendicular to the missile axis. In computing flows around canard-controlled missiles, it can be very important to avoid excessively dissipating the canard vortices as they convect the length of the missile body. To provide this resolution, the mesh has a pre-specified adaptation region covering the entire missile, and within this region the mesh is refined 3 levels further driven by surface curvature as described in [5]. In addition to the canard vortices, a pre-specified adaptation region is designed to capture the shocks generated by many of the surface features on the missile body. Since streamlines passing through these shocks will impact the spinning fins, resolution and propagation of these shocks may be important. Resolution requirements for the baseline mesh were established using guidelines from previous simulations of canard-controlled missiles[10], and by performing a mesh resolution study with the current geometry. As the missile tail spins over the course of the simulation the mesh responds to track the body motion, re-adapting to the new geometry at each timestep (cf. [9, 10]). The snapshot shown here has approximately 4 million cells, and this total number of cells remains roughly constant over the course of a dynamic simulation with the tail section spinning.

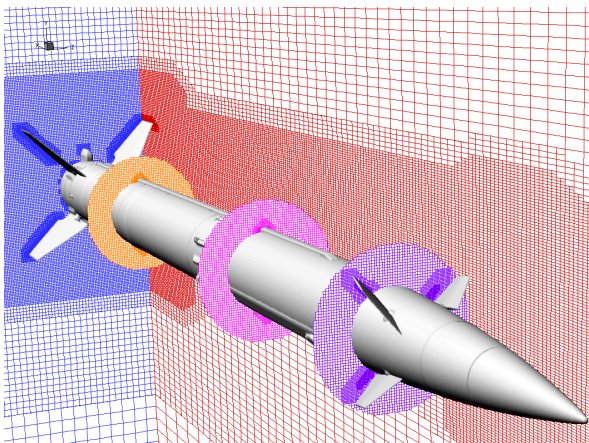


Figure 3: Cutting planes through the non-body-fitted Cartesian mesh used in simulations. Missile is shown with fins in the \times position and canards deflected asymmetrically $\delta_c = 16^\circ$. 4M Cartesian cells.

2.2 Cartesian Moving-Body Flow Solver

In order to simulate a missile with a spinning tail section, a scheme that allows rigid bodies to move relative to each other during a simulation is needed. A general numerical scheme for solving time-dependent flows with (optional) rigid-body motion for unstructured Cartesian meshes was developed from the parallel, steady-state solver described in [15]. A brief overview of the scheme will be presented here, and complete details can be found in [9].

2.2.1 Dual-time formulation

Extension of the steady-state flow solver to time-dependent flows was accomplished using a dual-time formulation (cf. Refs. [16, 17]),

$$\begin{aligned} \frac{d\mathbf{Q}}{d\tau} + R^*(\mathbf{Q}) &= 0 \\ R^*(\mathbf{Q}) &= \frac{\partial \mathbf{Q}}{\partial t} + R(\mathbf{Q}) \end{aligned} \quad (1)$$

where τ is referred to here as “pseudo-time”, and is the iterative parameter, and t is the physical time. \mathbf{Q} is the vector of conserved variables, and $R(\mathbf{Q})$ is an appropriate numerical quadrature of the flux divergence, $\frac{1}{V} \oint_S \mathbf{f} \cdot \mathbf{n} dS$. As $\frac{d\mathbf{Q}}{d\tau} \rightarrow 0$ the time-dependent formulation is recovered. The parallel multi-grid solver described in [15] is used to efficiently converge the inner pseudo-time integration. This is similar to the scheme outlined by Jameson[18], however, the semi-implicit approach of Melson et al.[19] is used here for the physical time-derivative term.

Various time-dependent schemes can be constructed for Eqn. 1 by appropriately discretizing the time derivative. In the current work, it’s desirable to use an unconditionally-stable, implicit scheme to allow a large timestep to be chosen based upon physical considerations rather than a potentially smaller stability-limited timestep. In the Cartesian embedded-boundary scheme, the cut-cell polyhedra can have arbitrarily small volumes, and a stability limit can be very restrictive. Using a large timestep also reduces the amount of computational work required to process the moving geometry and mesh through a complete simulation. In the current work, the backward Euler and 2nd-order backward time-integration schemes have both been utilized.

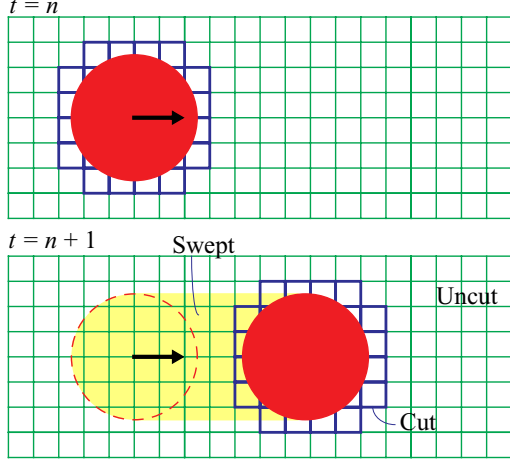


Figure 4: Schematic of a rigid-body moving through a Cartesian mesh. Cells cut by the geometry at each timestep are outlined in blue, and cells swept by the geometry over the timestep are tinted yellow.

2.2.2 Relative motion

Figure 4 shows a schematic of a rigid-body moving through a fixed Cartesian mesh over one discrete timestep. Cells cut at the beginning and end of the timestep are outlined in blue, and the shaded region highlights cells which have been “swept” by the body through the timestep. These swept cells change volume and shape over the timestep, and can appear or disappear (or both) as well. Away from the swept region, the cells don’t change and therefore require no special treatment. The swept-cells, however constitute the major challenge since the deformation of these cells over the timestep needs to be taken into account in order to satisfy the governing equations. The equations of motion for the deforming cells can be written in an integral conservation form as

$$\frac{d}{dt} \int_{V(t)} \mathbf{Q} dV = - \oint_{S(t)} \mathbf{f} \cdot \mathbf{n} dS \quad S = \partial V \quad (2)$$

$$\mathbf{f} \cdot \mathbf{n} = \begin{Bmatrix} \rho u_n \\ \rho u_n \mathbf{u} + p \mathbf{n} \\ \rho u_n e + p \mathbf{u} \cdot \mathbf{n} \end{Bmatrix}$$

$$u_n = (\mathbf{u} - \mathbf{w}) \cdot \mathbf{n}$$

Here \mathbf{w} is the velocity of the moving boundary with respect to the Eulerian frame.

Integrating the deforming-cell governing equations for a representative cell j using the backward-

Euler scheme gives

$$(\mathbf{Q}V)_j^{n+1} - (\mathbf{Q}V)_j^n - \sum_{ahead} (\mathbf{Q}V)^n = - \Delta t \sum_j (\hat{\mathbf{f}} \cdot \mathbf{n} \Delta S)^{n+1} \quad (3)$$

$\sum_{ahead} (\mathbf{Q}V)^n$ is a conservation correction term which represents the flux out of the swept cells over a timestep (cf. Ref. [9]). Equation 3 can be numerically integrated using the dual-time scheme outlined above. The terms $(\mathbf{Q}V)_j^n$ and $\sum_{ahead} (\mathbf{Q}V)^n$ become fixed source terms in the dual-time scheme. $(\mathbf{Q}V)^n$ however is only available on the mesh at time level n , while it is required on the mesh at time level $n+1$ in order to integrate Eqn. 3. $(\mathbf{Q}V)^n$ is conservatively transferred from the mesh at time level n to the new mesh at $n+1$ external to the flow solver. The transfer of the solution between two volumes meshes takes advantage of the space-filling-curve ordering of the cells in the Cartesian meshes (cf. Ref. [15, 20]). This allows the transfer to be performed very efficiently, requiring only two sweeps over the mesh cell list.

3 Numerical Results

The general 3-D Cartesian scheme outlined above is utilized to simulate the canard-controlled missile with spinning tail section described in Sec. 2.1. The Cartesian moving-body flow solver includes an interface for the GMP infrastructure[21]. This interface allows the entire analysis to proceed in a completely automated manner. The analyst defines a static configuration “space” of discrete tail orientations to calculate, defines a prescribed motion of the tail section for a dynamic simulation, and specifies a constrained 6-DOF simulation for the same tail section all through an interactive GUI application. These specified motions and states are then transferred to the flow solver and the static and dynamic analyses proceed in parallel without user intervention.

Since the flow conditions considered in this work are supersonic ($M_\infty = 1.6$), the geometry upstream of the tail section is static, and the tail section has horizontal and vertical symmetry, the flowfield within the tail section is periodic every 90° of spin. This periodicity was confirmed by the initial dynamic simulations. As such, it’s only necessary to simulate the motion of the tail section through 90° of rotation (after the initial transient). A baseline

angle of attack of $\alpha = 4.0^\circ$ is used to introduce the tail forced-spin-rate and free-to-spin approaches, as the canard/tail interactions are greatest at this angle of attack, leading to the highest tail spin rate. Next, the trends of the spinning tail section with angle-of-attack variation are examined by simulating $\alpha = 0.0^\circ$ and 12.0° , both with the tail held fixed and spinning.

3.1 Static Baselines

In order to provide a baseline for comparison with dynamic, spinning-tail computations, a series of static, steady-state simulations with the tail fixed at various (non-uniform) azimuthal orientations are undertaken for each configuration examined. A converged steady-state solution with the tail section in the \times configuration ($\phi_{tail} = 0^\circ$) is used to introduce the features of the flowfield in Fig. 5. Mach number contours at cutting planes along the longitudinal axis of the missile highlight the convection of the canard vortices. A schematic next to the contour planes shows the orientation and direction of spin of the vortices. The vortices shed from the tips of the NW, NE, and SE canards (following the compass directions viewed from the nose) convect down the length of the body. The vortex shed from the NE canard is stronger than the NW or SE vortices, as that canard is pitched up, while the other canards are pitched down. The vortex shed from the SW canard is “trapped” by the body as it convects upwards and dissipates. The asymmetric pitch of the canards causes an induced velocity which drives the vortices into the NE quadrant, where they impact the tail section. The induced velocity from the canards changes the local angle of attack seen by the tail fins, and the canard vortices also provide suction on the tail fins. This can be seen quantitatively in Fig. 6, where the variation of tail rolling moment with angle of rotation from the \times position is shown for a series of static solutions. A negative tail rolling moment would cause the tail section to rotate clockwise when viewed from the nose. As the tail fin approaches the (strongest) NE canard vortex, the tail rolling moment is strongest (near $\phi_{tail} = 80^\circ$). As the tail section moves to the $+$ position ($\phi_{tail} = 45^\circ$), the fins are farthest from the strong NE canard vortex, and evenly split (vortex suction inducing both CW and C-CW rotation) between the remaining two vortices, and the tail rolling moment is nearly the weakest. This differential pressure on the tail fin in the NE quad-

rant due to the vortices, along with the effects of dynamic pressure and angle of attack, and the induced velocity field from the canards all combine to impart a net rolling moment on the unconstrained tail, causing it to spin.

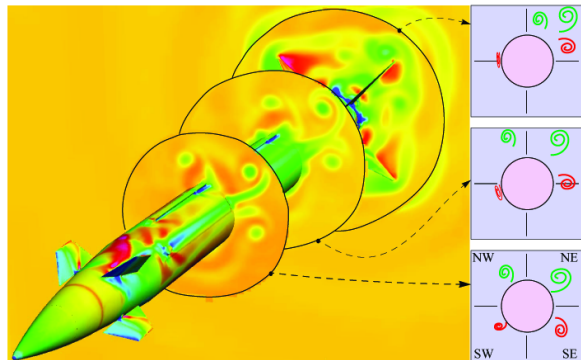


Figure 5: Mach number contours (blue is low, red is high) for a static simulation with tail in \times position. The schematic to the right shows the location and sense of rotation of the canard vortices. ($M_\infty = 1.6$, $\alpha = 4.0^\circ$).

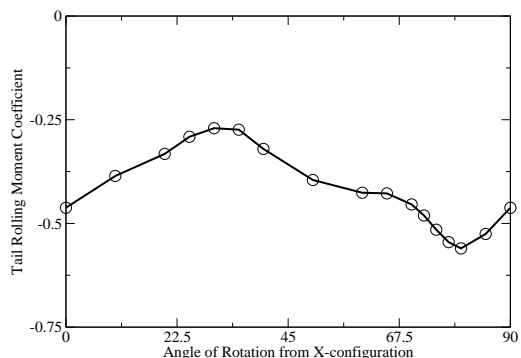


Figure 6: Tail rolling-moment for the static, fixed-tail simulations ($M_\infty = 1.6$, $\alpha = 4.0^\circ$).

3.2 Forced-spin-rate Tail Section

The rotation rate of the tail section is not known a priori. In order to determine the “natural” roll rate of the tail section – the rate at which the spin-averaged rolling moment on the tail is zero – an iterative process is used. First, it’s assumed that the tail rotation rate is low enough that the variation of spin-averaged tail rolling moment with rotation rate is linear. A fixed rotation rate is then imposed on the tail, which is intended to be a reasonable guess. The resulting spin-averaged tail rolling moment from this simulation, along with the static results discussed above (i.e. a zero-spin-rate simulation) are then fit with a straight line to determine

the predicted natural roll rate of the tail section. A second dynamic simulation is then performed at the natural roll rate in order to confirm the prediction.

An initial guess of 2500 rpm for the tail rotation rate was used at $\alpha = 4^\circ$. A time-resolution study was performed at this rotation rate using timesteps that move the tail fins 2° , 1° , 0.5° , 0.3° , and 0.15° of rotation per step respectively. The results of this time-resolution comparison showed no difference in tail load vs. rotation angle between the 0.3° and 0.15° of rotation/timestep simulations, and as a result 0.3° of roll per timestep was utilized for all of the simulations discussed here. This timestep is smaller than preferred for computational efficiency in a dual-time scheme, but is required to accurately capture the complex physics with the current numerical scheme.

Figure 7 shows the spin-averaged tail rolling moment against the imposed rotation rate for the iterative process discussed above. The variation of averaged tail rolling moment with rotation rate is confirmed to be linear, and the predicted natural rotation rate is 2155 rpm for these conditions. The variation of tail rolling moment with rotation angle is shown in Fig. 8 for all computations; the static and the two dynamic with an imposed rotation rate. The simulation with the natural rotation rate does provide nearly zero spin-averaged tail rolling moment ($C_{l_{tail}} = -0.008$). As the canard vortices, canard downwash, and wind vector do not change when the tail spins, the variation of tail rolling moment with rotation angle is similar for all simulations, however shifted as the rotation rate increases. This implies that the rotation of the tail section provides minor dynamic effects, and these effects wash downstream without influencing the aerodynamic loads. This is especially true with a fixed spin rate as there is no acceleration of the tail section. When the velocity of the tail section “balances” the outer flow effects, a stable spin rate is found. Since the variation in tail rolling moment is self-similar with fixed spin rates, it is unnecessary to compute the entire cycle at the initial guess. Once the increment between the static and initial guess is known, i.e. after the transient portion of the cycle has been computed, this increment can simply be applied to the static spin-average to obtain the spin-average at the initial guess. This technique was applied successfully at $\alpha = 12.0^\circ$, the results of which will be discussed Sec. 3.4.

Mach number contours through the tail section,

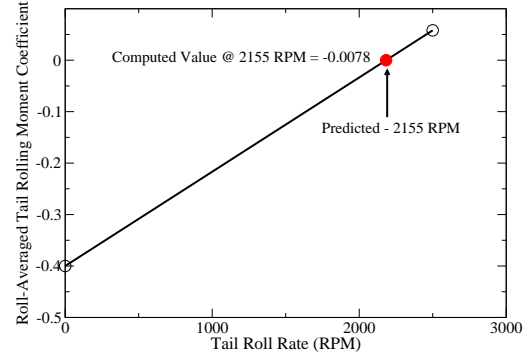


Figure 7: Predicted “natural” tail rotation rate ($M_\infty = 1.6$, $\alpha = 4.0^\circ$).

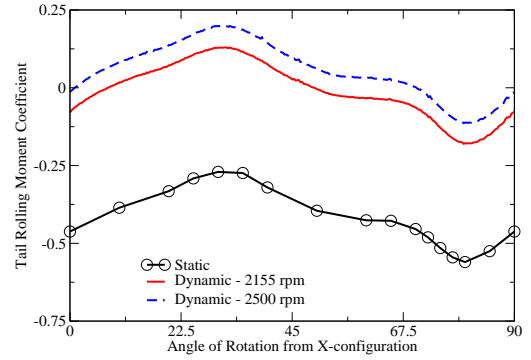
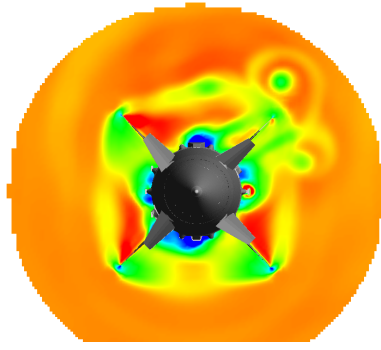


Figure 8: Tail rolling-moment for static, fixed-tail and dynamic, forced-spin-rate simulations ($M_\infty = 1.6$, $\alpha = 4.0^\circ$).

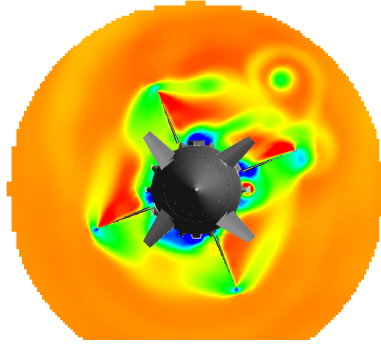
viewed from the nose, are shown in Fig. 9 for the natural rotation rate - 2155 rpm. As the fins encounter the vortices there is a strong interaction, however after the fins pass the vortices reform in their original positions. A similar series of pressure contours on the surface of the tail section is shown in Fig. 10. The shocks emanating from the complex geometry upstream interact with the tail section as it rotates. The narrow gaps and clearances in the geometry provide no difficulty for the current method.

3.3 Free-to-spin Tail Section

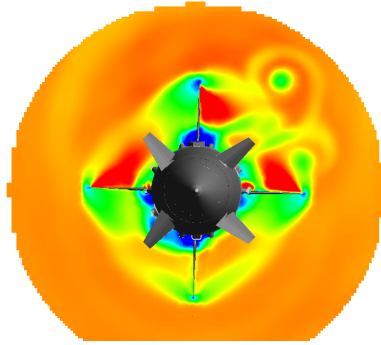
The forced-spin tail is an approximation to the actual rotation of the tail section. The actual motion will respond to the aerodynamic forces as it spins, and increase or decrease the spin-rate accordingly. In order to assess the efficiency and accuracy of the forced-spin approximation, simulations with a free-to-spin tail were performed using the coupled CFD/6-DOF method outlined in [22]. The 6-DOF motion is constrained to only allow rotation about the longitudinal axis of the missile body, effectively



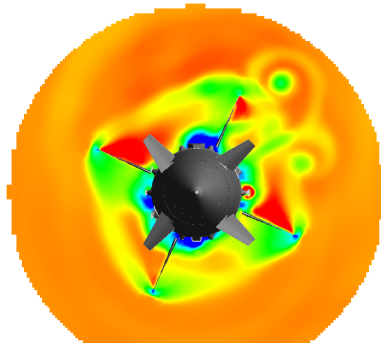
(a) $\phi_{tail} = 0.0^\circ/90.0^\circ$



(b) $\phi_{tail} = 22.5^\circ$

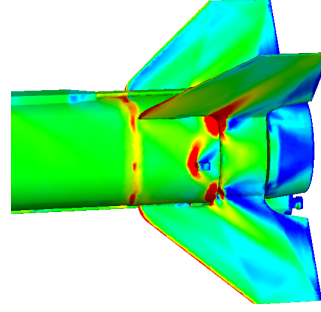


(c) $\phi_{tail} = 45.0^\circ$

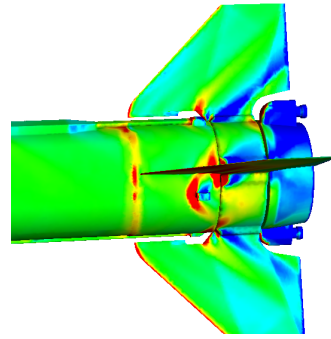


(d) $\phi_{tail} = 67.5^\circ$

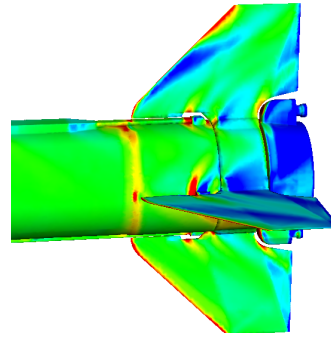
Figure 9: Velocity magnitude contours through the tail section (red is high, blue is low) viewed from the nose ($\phi_{tail} = 2155$ rpm, $M_\infty = 1.6$, $\alpha = 4.0^\circ$).



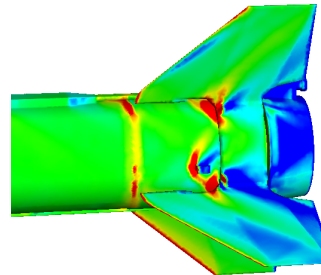
(a) $\phi_{tail} = 0.0^\circ/90.0^\circ$



(b) $\phi_{tail} = 22.5^\circ$



(c) $\phi_{tail} = 45.0^\circ$



(d) $\phi_{tail} = 67.5^\circ$

Figure 10: Surface pressure contours on the tail section (red is high, blue is low). ($\phi_{tail} = 2155$ rpm, $M_\infty = 1.6$, $\alpha = 4.0^\circ$).

limiting this to a 1-DOF simulation. The actual inertia of the tail section is unknown, and is approximated by assuming the density of the tail section to be half the density of aluminum (i.e. assume that the tail section is partially hollow). This assumed uniform density is used with the surface geometry to provide an estimate of the rotational inertia required for the 1-DOF simulations (cf. Mirtich[23]).

The 1-DOF simulations were initiated from the 2155 rpm forced-spin simulation. As expected, the motion of the tail immediately responds to the aerodynamic forces, and the spin rate of the tail begins to vary (cf. Fig. 11). The average spin-rate of the tail increases every quarter-revolution the tail completes. Note that the 2155 rpm simulation does predict a small negative tail rolling moment, i.e. predicts that the tail is spinning slightly too slow. The change in average spin-rate each quarter cycle is less than 0.5% of the mean spin rate, and likewise the maximum deviation from the mean rate over each cycle is only $\pm 0.5\%$. Even with these small variations in spin-rate, the aerodynamic loads on both the tail section and the entire missile are periodic after an initial transient lasting roughly 45° of tail rotation. The variation of tail rolling moment for the 1-DOF free-to-spin simulation is compared to the 2155 rpm forced-spin-rate simulation and the static simulation in Fig. 12. The tail load variation closely follows the forced-spin variation, since the tail acceleration is moderate throughout, however the amplitude of the load variation in the free-to-spin simulation is lower as the tail responds to the aerodynamic forces.

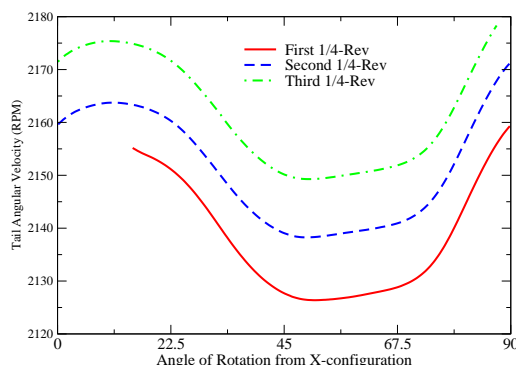


Figure 11: Tail angular velocity for free-to-spin (1-DOF) simulation. ($M_\infty = 1.6$, $\alpha = 4.0^\circ$).

Since the loads on the tail and the entire missile are periodic, even though the spin-rate is still changing slightly, meaningful spin-averages can be computed for comparison with the forced-spin sim-

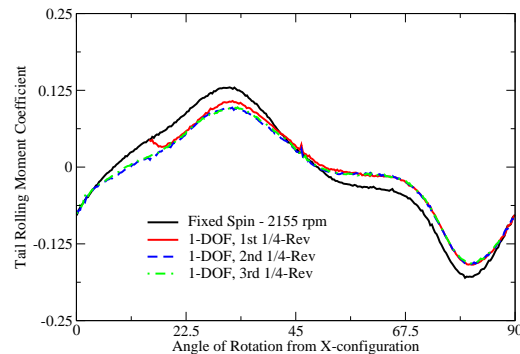


Figure 12: Tail rolling-moment for forced-spin and free-to-spin simulations ($M_\infty = 1.6$, $\alpha = 4.0^\circ$).

ulations. The spin-averaged forces and moments on the missile for the forced-spin and 1-DOF simulations are presented in Table 1. The maximum difference in spin-averaged loads between the forced-spin and 1-DOF simulations is 6%. At these conditions the changes in spin-rate over each cycle, and by inference the dynamic effects due to the acceleration of tail, are both small. Hence the more computationally-efficient forced-spin technique can be used in place of a full free-to-spin simulation. The spin-average can be computed in little more than a single quarter-revolution with the forced-spin approximation, while the free-to-spin simulations may take many revolutions to reach a stable state.

In order to provide more insight into the aerodynamics of the spinning-tail configuration, the $\alpha = 4.0^\circ$ static and dynamic (both fixed- and free-to-spin) results are analyzed using a plot of the crossflow moments (Fig. 13). Here the yawing and pitching moments are plotted on the two axes as the tail spins, along with the spin-averaged values. In order to make performance predictions, the spin-averaged forces and moments of the dynamic configuration are required. While one static configuration does closely predict the dynamic spin-averaged loads, this is fortuitous, and different canard settings or flow conditions will behave differently. The dynamic curves are shifted up and to the right from the static curve, and maintain the shape basic shape. This self-similarity is due to the lack of dynamic effects. The tail provides a “restoring” moment opposite to the effect the canards provide ahead of the center of mass. When the tail is free to spin, this restoring moment is reduced as the tail moves in response to the aerodynamic forces. From this point of view, the free-spinning tail behaves as if it was an equivalent static tail of smaller

size. Hence the increment between the static and dynamic simulations is in the direction the canards are forcing the body to rotate, in this case nose up and starboard.

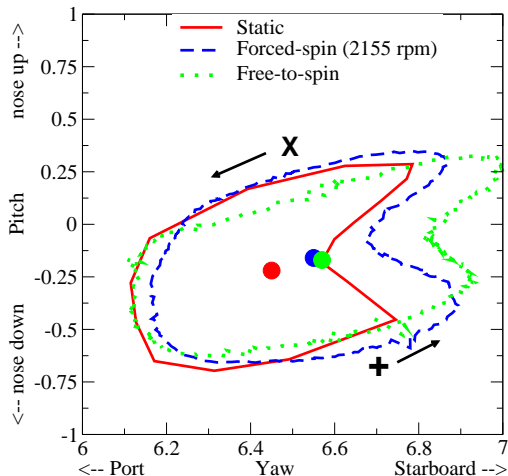


Figure 13: Crossflow moments for the static and dynamic simulations. Spin-averaged values are shown with solid circles. The \times and $+$ positions are labeled, along with the direction of tail spin. ($M_\infty = 1.6$, $\alpha = 4.0^\circ$).

Table 1 compares the current inviscid simulations at $\alpha = 4.0^\circ$ with high-resolution, viscous, free-to-spin simulations computed by Nygaard[11] for the same missile configuration. The computed spin-averaged forces and moments for both free-to-spin simulations are all within 2.5%, with the exception of pitching moment.*

3.4 Variation with Angle of Attack

The previous sections outline the aerodynamics of the free-spinning tail section, along with a methodology for predicting the behavior using a forced-spin approximation at $\alpha = 4.0^\circ$. This section will extend the analysis by considering the behavior at $\alpha = 0.0^\circ$ and 12.0° . First, static solutions were computed with the tail in fixed azimuthal locations to complement the results presented previously for $\alpha = 4.0^\circ$ in Fig. 6. The variation of tail rolling moment from these series of static simulations is presented in Fig. 14. As expected, the computations at $\alpha = 4.0^\circ$ show the highest magnitude tail rolling moment, as the canard/tail interactions are strongest at this angle of attack. Correspondingly, the variation at $\alpha = 4.0^\circ$ never changes sign, so that the tail will spin clockwise regardless of the

initial tail orientation. This differs from the results at $\alpha = 0.0^\circ$ and 12.0° , which both show statically-stable tail orientations near $\phi_{tail} = 45.0^\circ$ and 22.5° respectively. The spin-averaged tail rolling moment for $\alpha = 0.0^\circ$ is zero since the flowfield is symmetric with respect to the horizontal plane, while the spin-averaged tail rolling moment at $\alpha = 12.0^\circ$ is not. Whether these statically-stable positions are also dynamically-stable to small perturbations is unknown, however it is almost certain that some conditions (angle of attack, canard setting, ...) do provide regions of local dynamic stability. The implications of this will be discussed after the dynamic simulations at $\alpha = 12.0^\circ$ are presented.

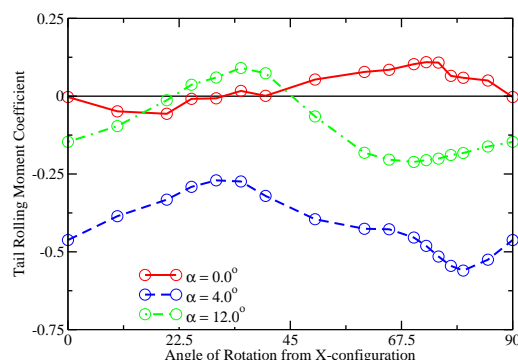


Figure 14: Tail rolling-moment for static simulations at all angles of attack. ($M_\infty = 1.6$).

Since the static results at $\alpha = 12.0^\circ$ indicate a non-zero spin-averaged tail rolling moment, the forced- and free-to-spin analysis described in the previous sections is applied at $\alpha = 12.0^\circ$ to provide insight. The forced-spin iterative method predicts a tail spin rate of near 500 rpm at $\alpha = 12.0^\circ$. Dynamic forced-spin results were obtained at this rate, and a 1-DOF free-to-spin simulation was initiated from the fixed-rate computation and continued through two quarter-revolutions. The tail spin rate for the free-to-spin simulation at $\alpha = 12.0^\circ$ is shown in Fig. 15, after the initial release from the 500 rpm forced-spin simulation. The mean tail spin rate increases by a small amount each quarter-revolution, but in contrast to $\alpha = 4.0^\circ$, the rotation rate varies by $\pm 10\%$ over each cycle - a factor of 20 more than the variation in Fig. 11. This large variation in tail spin rate is caused by the torque being applied over a longer time duration at this lower spin rate, and indicates that a forced-spin simulation at a fixed rate is *not* a good approximation for the actual motion at this angle of attack if the tail is spinning. Note that even though the

*The differences in axial force are not considered as the inviscid results are not corrected for viscous drag.

	C_A	C_Y	C_N	C_l	C_m	C_n
Static	0.48	0.65	1.11	-0.40	-0.22	6.45
Fixed-spin (2155 rpm)	0.53	0.61	1.12	-0.01	-0.16	6.55
Free-to-spin	0.50	0.61	1.12	0.00	-0.17	6.57
Free-to-spin Ref. [11]	0.69	0.60	1.15	-0.01	-0.04	6.49

Table 1: Computed spin-averaged forces and moments on the entire missile. All values are provided using standard aircraft coordinates. Axial force does not include the missile base section. ($M_\infty = 1.6^\circ$, $\alpha = 4.0^\circ$).

static results indicate a statically-stable tail orientation, the mean tail rotation rate still increases. The large variation in tail spin rate implies that the simulation contains large dynamic effects. This is seen in the crossflow moments plotted in Fig. 16. The static and dynamic forced-spin results are very close, as anticipated with this low spin rate, however the free-to-spin simulation predicts a large increment, and no longer maintains a shape similar to the static result. This change in shape is caused by the accelerations on the tail altering the dynamic flowfield from the static or forced-spin results. Since the shape of the crossflow plot can change almost arbitrarily under these conditions it is not reliable to use a simpler approximation, such as static or forced-spin, and apply a post-processing correction.

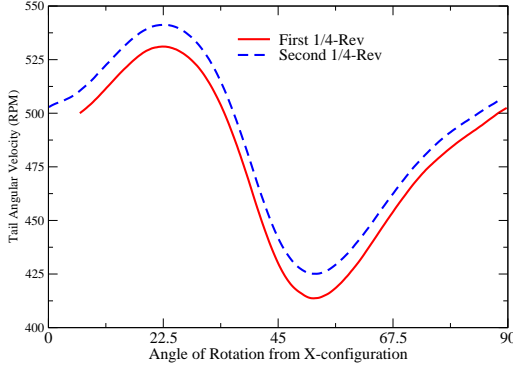


Figure 15: Tail angular velocity for free-to-spin (1-DOF) simulation. ($M_\infty = 1.6$, $\alpha = 12.0^\circ$).

The behavior of the tail rolling moment with varying angle of attack indicates that the actual behavior of the tail section is likely multi-valued. The results at $\alpha = 12.0^\circ$ demonstrate the possibility that a fixed tail orientation can be stable, while at the same time indicate strongly that an initially spinning configuration may not decay (stop spinning) at this same angle of attack. This implies that the state of the tail section at any time, and by inference the loads on the missile, is dependent upon the past time history of the missile configu-

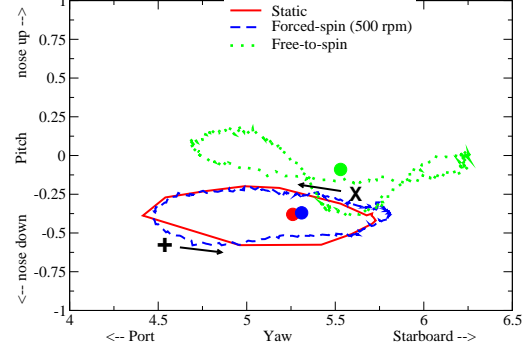


Figure 16: Crossflow moments for the static and dynamic simulations. Spin-averaged values are shown with solid circles. The \times and $+$ positions are labeled, along with the direction of tail spin. ($M_\infty = 1.6$, $\alpha = 12.0^\circ$).

ration. Depending upon the initial state and the path through time, different behavior can be observed. For example, in the current configuration at $\alpha = 12.0^\circ$, if the canards are initially undeflected, the flow will be symmetric and the tail will not be spinning. If the canards are then deflected, it's plausible that the tail section will remain fixed at the static stability point. However, if the canards are initially deflected at $\alpha = 4.0^\circ$ so that the tail is spinning at a high rate, and the body is pitched up to $\alpha = 12.0^\circ$, then it is plausible that the tail will remain spinning. Without knowledge of this time history it cannot be predicted in general whether to use a static analysis, a forced-spin analysis, or a full free-to-spin simulation. Further, the state of the spinning tail is also dependent upon its inertial properties. Note that this requires the inertial properties of a wind tunnel model to be scaled appropriately to predict the correct dynamic behavior of the actual system. Based upon the current results, the tail section can remain fixed, can rotate constantly, or could continually oscillate between the extremes of fixed and rotating tails. All of these behaviors have been observed during unpublished experimental tests of the current configuration.

4 Summary

The canard-controlled missile with a free-spinning tail section considered in the current work provides a difficult challenge for CFD methods. The geometry is extremely complex, and contains many scales and small clearances which must be resolved. The physics of the canard/tail interaction requires a significant volume mesh resolution, which places an emphasis on the efficiency of any solution process. Finally, in general the dynamic tail section requires a moving-body flow solver coupled with a 6-DOF module in order to provide an accurate analysis. An automated 3-D Cartesian method for analyzing complex geometries with components in relative motion has been demonstrated. The complete CFD solution process is automated: a surface triangulation is automatically generated from a CAD solid model, the volume mesh is automatically generated using the Cartesian scheme, and the dynamic flow solver is robust and efficient, and can handle any general rigid-body motion through a simple interface.

Three levels of fidelity were applied to analyze the missile with spinning-tail section at $M_\infty = 1.6^\circ$: a series of static simulations with the tail in fixed azimuthal orientations, a forced-spin dynamic simulation using an iterative approach to determine an appropriate fixed spin-rate, and a free-to-spin simulation using a flow solver coupled with a constrained 6-DOF module. The analysis of the spinning-tail configuration indicates that the choice of a static, forced-spin, or free-to-spin analysis cannot in general be made a priori. Attempting to correct low-fidelity results in a post-processing phase is also not possible in general due to the large dynamic effects which the spinning-tail configuration can generate. A variation in tail rolling moment can indicate regions of static stability, however this same variation can imply that an initially spinning tail will continue to spin. Further, the behavior of the dynamic tail section is likely multi-valued, and hence the state for any configuration is dependent upon the past history of the missile and its actual inertial properties. The investigation indicates that the tail section can remain fixed, can rotate constantly, or could continually oscillate between the extremes of fixed and rotating tails, and that all of these behavior could plausibly occur at the same flow conditions and control surface settings depending upon the previous history. The detailed information from a CFD analysis provides

the insight which is required to understand, and ultimately predict, the behavior of such a complex system.

Acknowledgments

The authors would like to thank Dr. Tor Nygaard of ELORET for providing the results of the viscous simulations, and Dr. Robert Meakin of the U.S. Army AFDD for providing the software to compute the inertial properties of the tail section. The authors would also like to thank Prof. Marsha Berger of the Courant Institute for her many insightful discussions on Cartesian methods.

References

- [1] Berger, M.J. and LeVeque, R., "Cartesian Meshes and Adaptive Mesh Refinement for Hyperbolic Partial Differential Equations," in *Proceedings of the 3rd International Conference on Hyperbolic Problems*, (Uppsala, Sweden), 1990.
- [2] Quirk, J., "An Alternative to Unstructured Grids for Computing Gas Dynamic Flows Around Arbitrarily Complex Two Dimensional Bodies," ICASE Report 92-7, 1992.
- [3] Karman, S.L. Jr., "Splitflow: A 3D Unstructured Cartesian/Prismatic Grid CFD Code for Complex Geometries," AIAA Paper 95-0343, 1995.
- [4] Melton, J.E., Berger, M.J., Aftosmis, M.J., and Wong, M.D., "3D Applications of a Cartesian Grid Euler Method," AIAA Paper 95-0853, 1995.
- [5] Aftosmis, M.J., Berger, M.J., and Melton, J.E., "Robust and Efficient Cartesian Mesh Generation for Component-Based Geometry," AIAA Paper 97-0196, Jan. 1997. Also *AIAA Journal* 36(6): 952-960, June 1998.
- [6] Wang, Z.J., Przekwas, A., and Hufford, G., "Adaptive Cartesian/Prism Grid Generation for Complex Geometry," AIAA Paper 97-0860, Jan. 1997.
- [7] Bayyuk, S.A., Powell, K.G., and van Leer, B., "Computation of Flows with Moving Boundaries and Fluid-structure Interactions," AIAA Paper 97-1771, 1997.

- [8] Lahur, P.R. and Nakamura, Y., "Simulation of Flow around Moving 3D Body on Unstructured Cartesian Grid," AIAA Paper 2001-2605, June 2001.
- [9] Murman, S.M., Aftosmis, M.J., and Berger, M.J., "Implicit Approaches for Moving Boundaries in a 3-D Cartesian Method," AIAA Paper 2003-1119, Jan. 2003.
- [10] Murman, S.M., Aftosmis, M.J., and Berger, M.J., "Numerical Simulation of Rolling-Airframes Using a Multi-Level Cartesian Method," AIAA Paper 2002-2798, June 2002.
- [11] Nygaard, T. A., "Aeromechanic Analysis of a Missile with Freely Spinning Tailfins," AIAA Paper 2003-3672, June 2003.
- [12] Haimes, R. and Aftosmis, M.J., "On Generating High Quality "Water-tight" Triangulations Directly from CAD," in *Meeting of the International Society for Grid Generation (ISGG) 2002*, June 2002.
- [13] Haimes, R. and Follen, G., "Computational Analysis Programming Interface," in *Proceedings of the 6th International Conference on Numerical Grid Generation in Computational Field Simulations*, (University of Greenwich), June 1998.
- [14] Aftosmis, M.J., Delanaye, M., and Haimes, R., "Automatic Generation of CFD-ready Surface Triangulations from CAD Geometry," AIAA Paper 99-0776, Jan. 1999.
- [15] Aftosmis, M.J., Berger, M.J., and Adomavicius, G., "A Parallel Multilevel Method for Adaptively Refined Cartesian Grids with Embedded Boundaries," AIAA Paper 2000-0808, Jan. 2000.
- [16] Merkle, C.L. and Athavale, M., "A Time Accurate Unsteady Incompressible Algorithm Based on Artificial Compressibility," AIAA Paper 87-1137, June 1987.
- [17] Rogers, S.E., Kwak, D., and Kiris, C., "Numerical Solution of the Incompressible Navier-Stokes Equations for Steady-State and Time-Dependent Problems," AIAA Paper 89-0463. Also *AIAA Journal* **29**(4):603–610, 1991.
- [18] Jameson, A., "Time Dependent Calculations Using Multigrid with Applications to Unsteady Flows Past Airfoils," AIAA Paper 91-1596, June 1991.
- [19] Melson, N.D., Sanetrik, M.D., and Atkins, H.L., "Time-accurate Navier-Stokes Calculations with Multigrid Acceleration," in *Proceedings of the Sixth Copper Mountain Conference on Multigrid Methods*, Apr. 1993.
- [20] Aftosmis, M.J., Berger, M.J., and Murman, S.M., "Applications of Space-Filling-Curves to Cartesian Methods for CFD," submitted to AIAA ASM Conference, Reno, NV, Jan. 2004.
- [21] Murman, S.M., Chan, W.M., Aftosmis, M.J., and Meakin, R.L., "An Interface for Specifying Rigid-Body Motion for CFD Applications," AIAA Paper 2003-1237, Jan. 2003.
- [22] Murman, S.M., Aftosmis, M.J., and Berger, M.J., "Simulations of 6-DOF Motion with a Cartesian Method," AIAA Paper 2003-1246, Jan. 2003.
- [23] Mirtich, B., "Fast and Accurate Computation of Polyhedral Mass Properties," *Journal of Graphics Tools*, 1(2):31–50, 1996.